metals

MDPI

Article

Tensile and Fatigue Analysis Based on Microstructure and Strain Distribution for 7075 Aluminum FSW Joints

Guoqin Sun [1,*], Xinhai Wei [1], Deguang Shang [1], Shujun Chen [1], Lianchun Long [1] and Xiuquan Han [2]

1 Faculty of Materials and Manufacturing, Beijing University of Technology, Beijing 100124, China; 18810816630@163.com (X.W.); shangdg@bjut.edu.cn (D.S.); sjchen@bjut.edu.cn (S.C.); longlc@bjut.edu.cn (L.L.)
2 AVIC Beijing Aeronautical Manufacturing Technology Research Institute, Beijing 100024, China; hanxq001@avic.com
* Correspondence: sguoq@bjut.edu.cn

Received: 26 October 2020; Accepted: 25 November 2020; Published: 30 November 2020

check for updates

Abstract: In order to study on tensile and fatigue fracture mechanism of friction stir welded (FSW) joints, the tensile and fatigue behavior of FSW joints are studied based on the microstructure and strain distribution. The large plastic deformation and fracture occurred in the thermo-mechanically affected zone (TMAZ) on retreating side in tension tests. High contents of shear texture and small angle grain boundary reduce the tensile mechanical property of TMAZ material. The fatigue weak area for FSW joints is affected by the loading condition. The strain concentration in the welded nugget zone (WNZ) and base material makes the fatigue fracture liable to happen in these areas for the FSW joints under the stress ratios of 0.1 and −0.3. When the fracture occurred in WNZ, the crack initiation mainly occurred in clusters of hardened particles, while when the fracture happened in base material, the crack initiation mainly occurred near the pit. The crack in WNZ propagated in an intergranular pattern and the crack in the other areas extended in a transgranular mode, leading to a higher crack growth rate of WNZ than of other regions.

Keywords: friction stir welding; microstructure; strain concentration; fracture location; crack propagation

1. Introduction

Friction stir welding (FSW) is widely used in aerospace, shipbuilding, automotive, and other industries. Fatigue fracture is the primary failure mode for FSW joints under variable load. The study of the fatigue characteristics of FSW joints is of great significance to understand its failure process and mechanism [1–5]. The material microstructure has an influence on its mechanical property, crack initiation, and propagation of welded joints. It is considered that the content and type of textures have an effect on the mechanical property of welded joints. The shear texture decreases the property of materials [6]. Fatigue crack mainly initiated around hardening particles, inclusion or intermetallic compounds [7–13]. Sun et al. [14] found that the initiation and propagation of small cracks are affected mainly by strengthening particles, grain boundaries, and rough pits for 7075 aluminum alloy FSW joints. Shou et al. noted that the grain size has a certain effect on fatigue crack growth rate of aluminum alloy [15]. Zheng et al. [16] studied the fatigue crack growth behavior of AA2524-T34 aluminum alloy. The crack tends to propagate along the grain boundary with low angular misorientation and deflect when it meets the grains with large-angle misorientation.

The hardness distribution of FSW joints generally presents the shape of "W" and the minimum hardness value is basically located in the thermo-mechanically affected zone (TMAZ) [17]. The distribution of hardness has an influence on tensile and fatigue fracture [17–21]. Rajakumar et al. [18] considered that tensile strength of aluminum alloy FSW joints exhibited a linear relationship with the hardness distribution of joint. A higher hardness of material generally obtains a higher tensile strength. However, the fatigue failure of FSW joint does not necessarily correspond to the hardness [22]. It also relates to the welding defects and applied load. The initiation and propagation of fatigue cracks are influenced by the evolution of microstructures, hardness distribution, and local strain [23]. A single factor might not accurately predict the fatigue fracture behavior of welded joints.

Tensile and fatigue fracture are prone to occur in the location with considerable strain. Digital image correlation (DIC) technology has been used to the strain measurement in tensile and fatigue tests for the welded joints [24–26]. The strain concentration area is prone to be the crack initiation position under fatigue load [27]. Peng et al. [28] verified the accuracy of DIC technique in strain characterization of welded joints by comparing with tensional strain data. Corigliano et al. [29] found that the changes of strain in different regions during the elastic stage are comparable. Malitckii et al. [30] revealed a cumulative deformation field at a subgrain level during small fatigue crack growth based on situ DIC image recording.

To further explore the influence of microstructure and strain distribution on tensile and fatigue properties of FSW joints, the tensile and fatigue behavior for 7075 aluminum FSW joints were studied using electron backscatter diffraction(EBSD) and DIC techniques. The effects of texture, hardness distribution, and strain variation on tensile and fatigue behavior of FSW joints were studied, and the difference of fracture mechanism was revealed.

2. Experiment

2.1. Specimen Preparation

The rolled 7075-T651 aluminum alloy plate with thickness of 3 mm was used in this study. The chemical composition and mechanical properties are presented in Tables 1 and 2. Elongation is the ratio of total deformation of the gage section to the original gage length after tensile fracture. The plates with dimension of 3 mm × 30 mm × 15 mm were cut and welded with a rotation speed of 800 rpm, a welding speed of 80 mm/min, and a tool titling angle of 2° along the direction perpendicular to the rolling direction. The FSW tool consists of a shoulder with a diameter of 10 mm and a stirring pin of 2.9 mm in length and 3.9 mm in diameter. Then, the specimens for tension and fatigue were wire cut and their axis direction was perpendicular to the welding line. The shapes and sizes of tensile and fatigue specimens were the same and referenced the Chinese national standard of GBT 228.1-2010, as shown in Figure 1. In order to observe the strain variation with DIC strain measurement device and crack propagation with metallographic microscope, the top and bottom surfaces of specimens were grinded with the sandpapers from 240 to 4000 grit and polished with the diamond pastes from w2.5 to w1 before tests. The smooth specimen after being grinded and polished is shown in Figure 2.

Table 1. Chemical compositions of 7075-T6 (wt %).

Zn	Mg	Cu	Mn	Ti	Cr	Fe	Si
5.59	2.40	1.49	0.10	0.072	0.23	0.20	0.225

Table 2. Mechanical property of 7075-T6 aluminum alloy.

Material	Ultimate Strength/MPa	Yield Strength/MPa	Elongation (%)
7075-T6	543	444	6

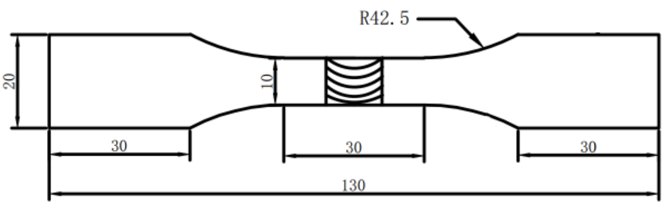

Figure 1. Shape and size of tensile and fatigue specimen. (Unit: mm).

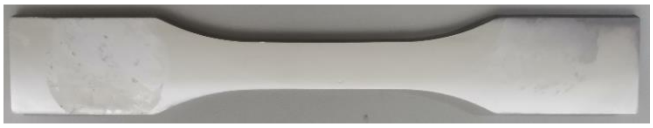

Figure 2. Smooth specimen after being grinded and polished.

2.2. Cross-Sectional Morphology

Figure 3 shows the cross-sectional morphology of 7075-T6 aluminum alloy FSW joint. The sample was taken from a welding plate centered on the weld and polished on the cross section of the sample. The welded joint is divided into different regions according to different microstructures due to different heat input and stirring action of stirring pin during the welding process. The regions of the welded joint are the weld nugget zone (WNZ), the thermo-mechanically affected zone (TMAZ), and the heat affected zone (HAZ). In addition, the welded joint is divided into advancing side (AS) where the direction of rotation linear speed is that of the welding advance and retreating side (RS) where the direction of rotation speed is opposite to the welding direction.

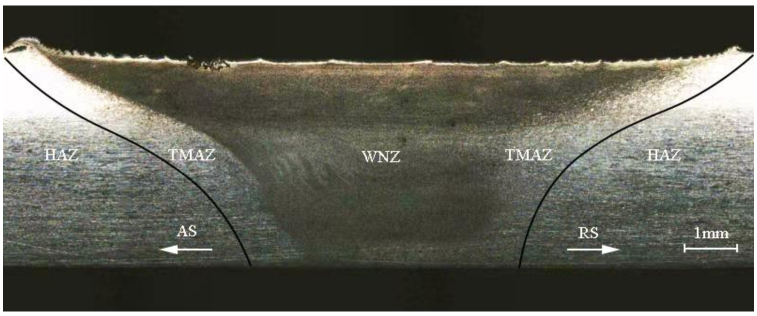

Figure 3. Cross-sectional morphology of the friction stir welded (FSW) joint.

2.3. Electron Backscatter Diffraction Analysis

The microstructure and the characteristics of cracks for FSW joint were observed with JEOLJSM 6500F electron backscatter diffraction (EBSD) microscope. Samples that contained different regions of welded joint were prepared, ground, mechanically polished, and electropolished before EBSD measurement. The electropolishing parameters with a solution of 30% nitric acid and 70% methanol are voltage of 12 V and polishing time of 60 s in a liquid nitrogen environment. The grain size, grain orientation, and texture distribution in each region of the joint were obtained with EBSD measurement.

2.3.1. Grain Size of Each Region

The grain size has an effect on the tensile property and fatigue crack growth of joints. According to the statistics, the average grain sizes of WNZ, TMAZ, HAZ, and base material (BM) are 2, 21, 71, and 68 microns, respectively. The grain size in WNZ is about one-thirtieth of that of BM. It rapidly increases 10-fold from WNZ to TMAZ. It was mentioned in [30] that the rapid change of grain size between WNZ and TMAZ caused the tensile failure at the junction of WNZ and TMAZ. The great change of grain size between WNZ and TMAZ leads to the degradation of performance at the junction of the two regions.

2.3.2. Grain Boundary Angle Distribution

The grain boundaries are divided into large angle and small angle grain boundaries according to the size of dislocation angle between adjacent grains. Generally, grain boundaries with small orientations ($\theta < 15°$) are called small angle grain boundaries and the grain boundaries with large orientations ($\theta > 15°$) are called large angle grain boundaries. Too much small angle grain boundary will decrease the material resistance to deformation. The grain boundary orientation angle distribution of each region of FSW joints is shown in Figure 4. The different colors denote different ranges of grain boundary orientation angle. The red lines represent large angle grain boundaries, the blue lines denote small angle grain boundaries, and the green lines in the grain are subgrain boundaries. The content of subgrain boundary in TMAZ is obviously higher than that in other regions [31]. The large number of subgrain boundaries decreased the proportion of large angle grain boundary in TMAZ, which indicated that the microstructure of TMAZ was seriously deformed. The proportion of large angle grain boundary in TMAZ is only 30%, which is much lower than that in BM, WNZ, and HAZ. Large angle grain boundary can hinder the slip deformation of crystals and promote the material strength at the grain boundary. The tensile strength will decrease if the number of small angle grain boundaries in TMAZ is too high.

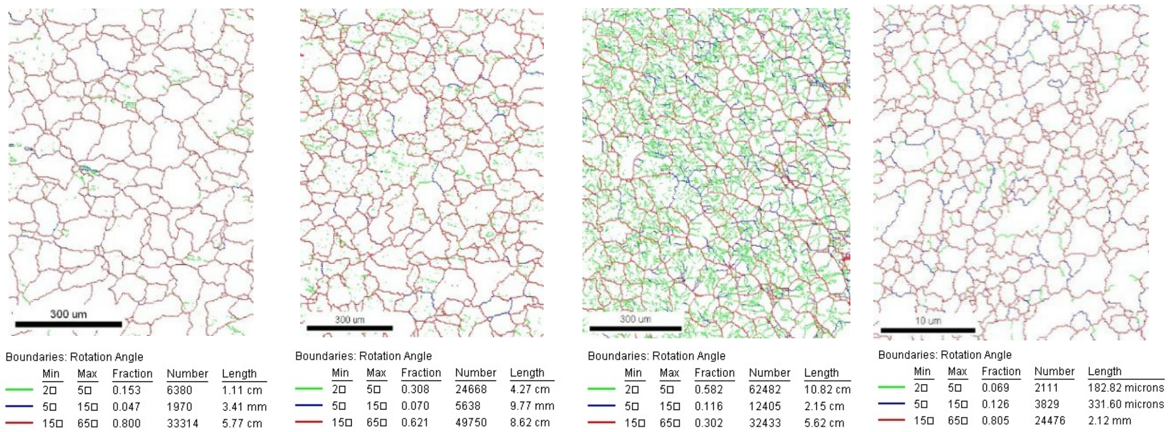

(**a**) (**b**) (**c**) (**d**)

Figure 4. Grain boundary orientation angle distributions of (**a**) base material (BM), (**b**) heat affected zone (HAZ), (**c**) thermo-mechanically affected zone (TMAZ), and (**d**) welded nugget zone (WNZ) in the FSW joint.

2.3.3. Orientation Distributions

The orientation distribution functions (ODFs) of different regions of welded joints are shown in Figure 5. The type and proportion of texture are listed in Table 3. Texture Cube {001} <100>, S {123} <634> texture, Brass {011} <211>, and Copper {112} <111>, all exist in each region of welded joint, as shown in Figure 5. The cubic texture Cube {001} <100> in BM and HAZ is strong and the contents reach 15% and 12.6%, respectively. High contents of texture Cube {001} <100> make the extreme densities of texture up to 26 and 19 in BM and HAZ. The high extreme density increases the strength of BM and HAZ and the preferred orientation distribution in BM and HAZ is obvious. The content of Goss texture {110} <001> in BM is higher than that of other regions. Goss texture improves the threshold value of fatigue crack growth, enhances the resistance of fatigue crack growth and effectively inhibits the initiation and propagation of cracks. The maximum extreme density of texture in TMAZ is reduced to 3.9. The content of shear texture {112} <110> in TMAZ is more than that of other textures. The texture {001} <110> is included in the shear texture also. Thus, the content of total shear texture in TMAZ reaches 2.4%. Excessive content of shear structure in TMAZ decreases the yield strength of material and a large plastic deformation is prone to happen in this region during the tensile process [32]. The type and content of texture are also related to the distribution of hardness. Excessive content of shear texture in TMAZ led to a hardness decrease to some degree [33]. The dynamic recrystallization occurred in WNZ during the welding process and the maximum extreme density in WNZ was decreased to 2.4. The strongest texture in WNZ is shear texture {112} <110>. The content of other textures is small and there is no obvious preferred orientation.

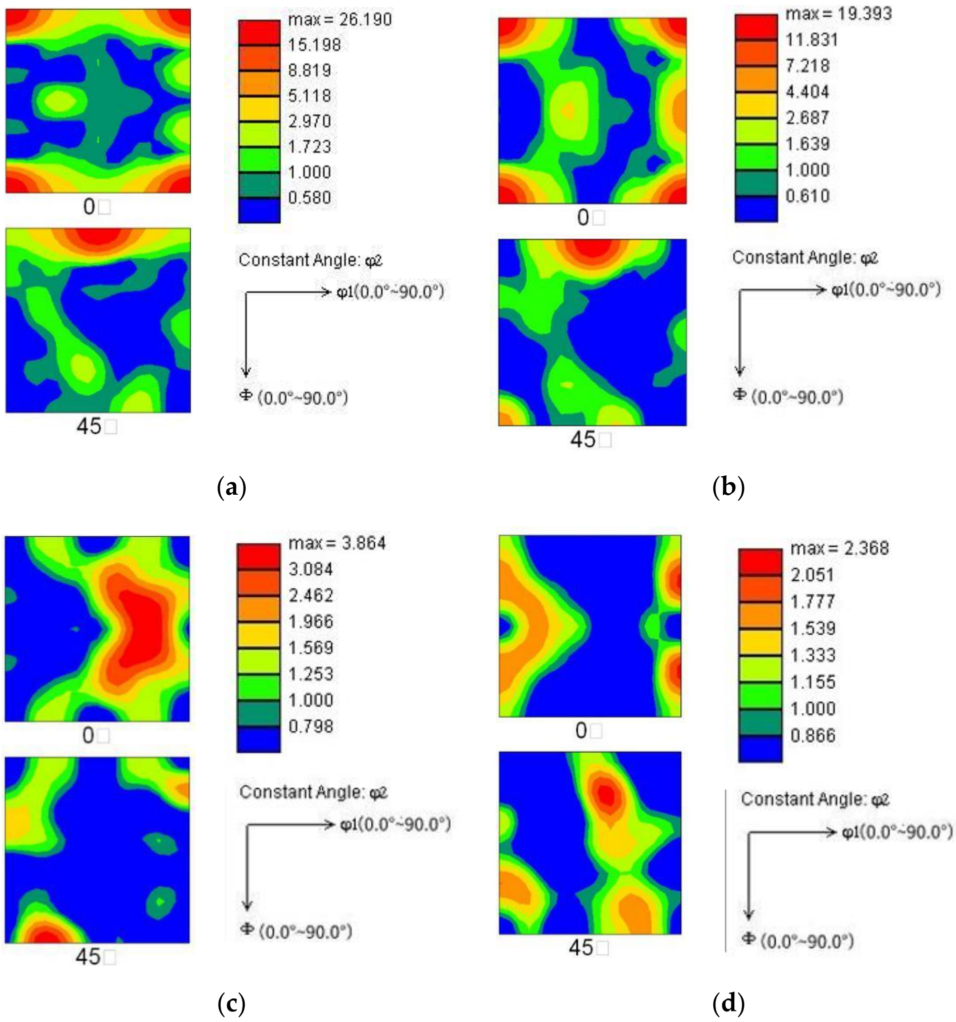

Figure 5. ODFs of (**a**) BM, (**b**) HAZ, (**c**) TMAZ, and (**d**) WNZ in the FSW joint.

Table 3. Texture type and proportion of different regions in FSW joint.

Type	Component	Base Material (BM)	Heat Affected Zone (HAZ)	Thermo-Mechanically Affected Zone (TMAZ)	Welded Nugget Zone (WNZ)
Deformation	Shear1 {001} <110>	0.1	0.1	0.5	0.1
	Shear3 {112} <110>	0.4	0.3	1.9	1.3
	Copper {112} <111>	1.1	0.1	0.4	0.2
	Brass {011} <211>	0.2	2.2	0.6	0.8
	Goss {110} <001>	1.7	0.1	0.8	0.5
	S {123} <634>	2	0.2	0.7	0.9
Recrystallization	Cube {001} <100>	15	12.6	0.4	1
	R {124} <211>	0.5	0.6	0.6	0.8

2.4. Hardness Distribution

The mechanical properties of the FSW joint are related to the hardness distribution. The hardness measurement was carried out with DHV-1000Z Vickers hardness tester. The hardness values were measured from the center of welding line to both sides with a 0.5 mm spacing at the distance from upper surface of 0.12 and 2.00 mm. The hardness distribution of FSW joint presents a "W" shape, as shown in Figure 6. Blue color represents low hardness region and red color denotes high hardness region. The hardness value decreases gradually from WNZ to TMAZ and then increases from TMAZ to BM. The hardness of BM is the largest and that of TMAZ is the smallest. The minimum hardness in TMAZ decreases by 40% compared with that of BM. Hardness distribution of WNZ is uniform, which suggests that the distribution of microstructure in this region is uniform. Previous studies have shown that there is a certain relationship between the hardness distribution of aluminum alloy FSW joint and the tensile fracture location [18,19]. The joints are prone to fracture in the region of low hardness. Therefore, the specimens are prone to fracture in TMAZ in tensile tests.

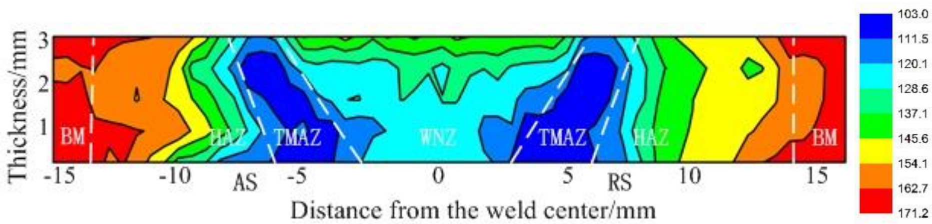

Figure 6. Hardness distribution of FSW joint.

3. Tensile Results Analysis Based on DIC Technique

The tensile tests were carried out with MTS-858 electro-hydraulic servo tester and the speed of axial displacement movement was 1 mm/min. VIC-3D DIC (Digital Image Correlation) strain measurement device was used to detect the strain at different regions of welded joint during tension test. The frequency of strain detection was set to twice per second. The strain maps of a joint specimen at different times were obtained after post processing. The strain curve of each region can be obtained by taking a point in each region of the FSW joint and the mechanical properties of the joint can be analyzed.

The relationship between strain concentration and tensile fracture of FSW joint was analyzed. Figure 7 shows the strain variation of the FSW joint under different stress levels during the tensile test process. Red color represents larger strain value and purple color expresses smaller strain value. In the stage of elastic loading, when the tensile stress was 140 MPa, the overall strain of the joint was smaller, as shown in Figure 7a. It can be considered that the performance of each region of welded joint is near uniform [29]. When the tensile stress achieved 470 MPa, the strain concentration region was located in TMAZ on both sides, which had been in a plastic stage. The strain in TMAZ increases with the increase of tensile stress. When the stress reached 530 MPa, the specimen fractured in TMAZ of RS. The TMAZ is softer than other regions in the joint, which is easier to produce a larger deformation than others. The largest strain happened in TMAZ and led to tensile fracture at TMAZ of the FSW joint, which was consistent with that of the description in [29].

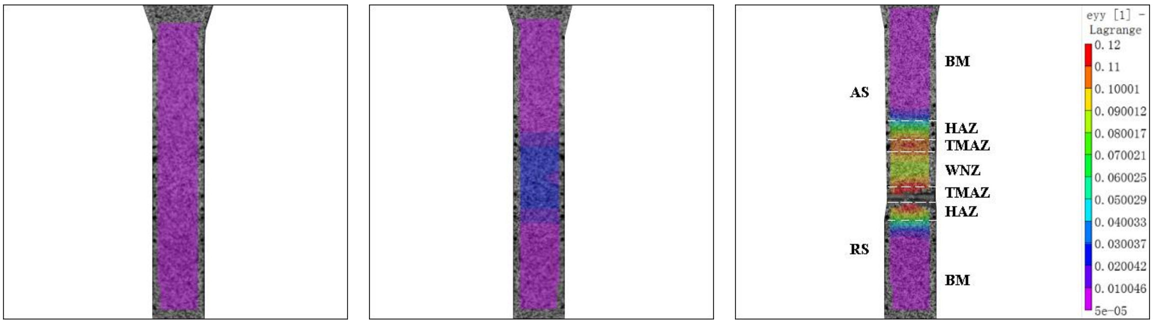

(**a**) (**b**) (**c**)

Figure 7. Tensile strains under tensile stresses of (**a**) 140 MPa, (**b**) 470 MPa, and (**c**) 530 MPa.

Figure 8 shows the stress–strain curves of each region in the FSW joint. The stress–strain curves in the elastic stage have little difference by comparison with that of BM. When the tensile stress reached about 420 MPa, the stress–strain curves of these regions changed greatly when the material entered the elastic-plastic stage. The strain in BM on both sides is small, followed by high hardness heat affect zone (HHAZ). The performance of these two regions is better than that of other regions from the analysis of stress–strain curves, which is consistent with the hardness distribution of FSW joint. The strain values in TMAZ and WNZ are larger during the plastic stage. The strain value of WNZ is 0.096, which is about 12 times of BM. Additionally, the maximum strain value in TMAZ on RS is 0.14, which is 18 times of BM. The material of TMAZ on RS had a large deformation during the tension process. Therefore, the tensile specimen fractured at TMAZ on RS.

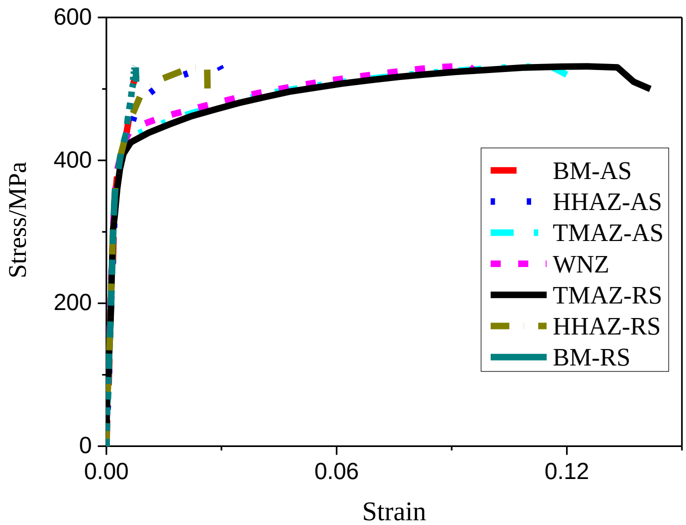

Figure 8. Stress–strain curves of the FSW joint.

4. Fatigue Experimental Analysis

4.1. Fatigue Experimental Results

In order to study the effect of loading parameters on fatigue life and fracture location of FSW joints, continuous fatigue tests with the stress ratios of 0.1 and −0.3 and frequency of 10 Hz were carried out on MTS-858 electro-hydraulic servo tester. The applied stress amplitude ranged from 90 to 157.5 MPa with the stress ratio of 0.1 and the applied stress is 99~171 MPa with the stress ratio of −0.3. The results of fatigue test for welded joints are listed in Table 4 [14]. It shows that the fatigue property decreases by comparison with the fatigue data of base material [34].

Table 4. Continuous and interrupted fatigue test data for FSW joints.

No.	Stress Amplitude /MPa	Stress Ratio	Frequency /Hz	Fatigue Life /Cycle	Fracture Location	Whether Test Interrupted
B3	157.5	0.1	10	21,766	WNZ	Continuous
B2	144	0.1	10	34,446	HAZ	Continuous
B1	126	0.1	10	45,447	BM	Continuous
B7	112.5	0.1	10	56,901	BM	Continuous
B8	99	0.1	10	61,618	WNZ	Continuous
B9	90	0.1	10	12,4278	TMAZ	Continuous
B5 *	157.5	0.1	10	28,453	WNZ	Interrupted
B7 *	157.5	0.1	10	18,808	WNZ	Interrupted
B6 *	144	0.1	10	25,053	WNZ	Interrupted
B13 *	126	0.1	10	37,508	WNZ	Interrupted
C18	171	−0.3	10	43,664	BM	Continuous
C2	157.5	−0.3	10	44,005	BM	Continuous
C7	144	−0.3	10	74,252	BM	Continuous
C3	126	−0.3	10	101,671	BM	Continuous
C10	112.5	−0.3	10	613,454	BM	Continuous
C18	99	−0.3	10	895,225	BM	Continuous
C17 *	171	−0.3	10	102,749	HAZ	Interrupted
C12 *	157.5	−0.3	10	26,787	WNZ	Interrupted
C16 *	144	−0.3	10	93,741	BM	Interrupted
D1 **	157.5	0.1	10	41,880	TMAZ	Interrupted
D2 **	144	0.1	10	22,010	TMAZ	Interrupted
D3 **	126	0.1	10	56,969	TMAZ	Interrupted

Note. The specimens marked * and ** are for the interrupted tests and the specimens marked ** are designed with the finest parts in HAZ and TMAZ. The detailed introduction are in Section 4.3.1.

The fatigue lives of FSW joints are greatly affected by loading stress and stress ratio. Figure 9 is the S-N curve obtained from the continuous fatigue experiments. It can be seen that the fatigue life decreases with the increase of loading stress. Under the same loading stress amplitude, the fatigue life under a stress ratio of −0.3 is generally higher than that under a stress ratio of 0.1.

The fatigue fracture location of joints is also affected by loading stress and stress ratio. Six of 10 specimens under the stress ratio of 0.1 fractured in WNZ. Seven of nine specimens under the stress ratio of −0.3 ruptured in BM. The statistical results of fracture location under different stress ratios are obtained from continuous and interrupted fatigue tests, as shown in Table 4. The fracture position of fatigue specimen under the stress ratio of −0.3 tends to move away from WNZ and most of them fracture in BM. Under the same stress amplitude, the applied maximum stress under the stress ratio of 0.1 is greater than that under the stress ratio of −0.3. It is considered that the loading stress has a great influence on the fracture position of FSW joint and the fracture location of the specimen tends to move toward WNZ with an increase of loading stress.

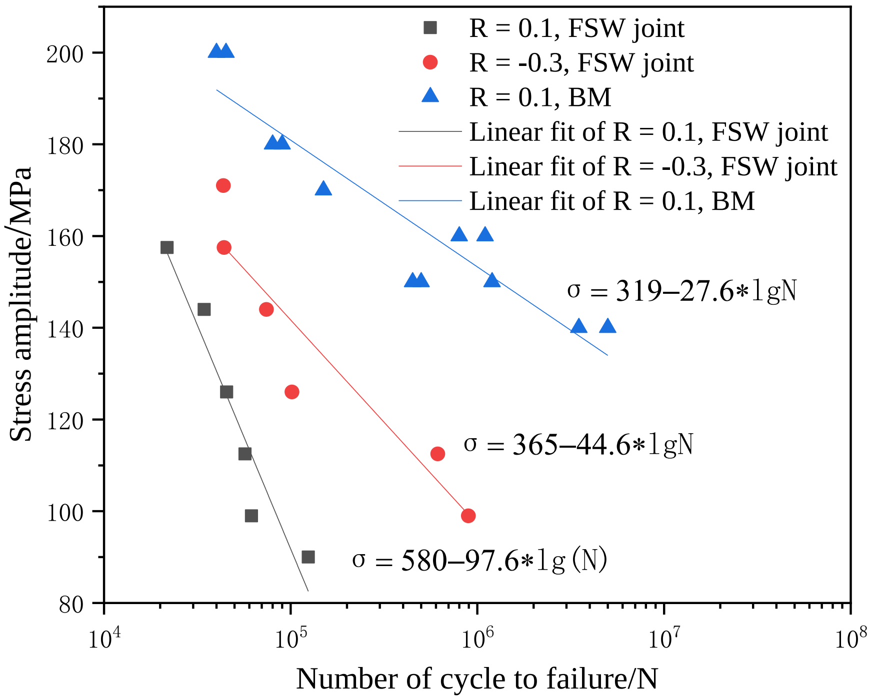

Figure 9. S-N curves of the FSW joint.

4.2. Strain Analysis

DIC technology was used to measure the strain of FSW joint in fatigue process, and the influence of strain on fatigue fracture was analyzed. The fatigue loading parameters are shown in Table 5.

Table 5. Fatigue test data of FSW joints based on strain analysis.

Specimen	Stress Amplitude (MPa)	Maximum Stress (MPa)	Stress Ratio	Frequency (Hz)	Fatigue Life (Cycles)	Fracture Position
E1	144	320	0.1	10	3574	WNZ
E2	126	193.8	−0.3	10	218,624	BM

The region of strain concentration tends to be the location of crack initiation under fatigue loading. Therefore, the location of fatigue crack initiation can be predicted by observing the region of strain concentration in fatigue tests [27]. The strains of FSW joints in the fatigue process are measured by the DIC technique for two specimens. The loading parameters of two samples are the maximum stress of 320 MPa with a stress ratio of 0.1 and the maximum stress of 193.8 MPa with a stress ratio of −0.3. Figures 10 and 11 show the strain distribution of specimens before fracture. Figure 10 shows the strain maps of specimen No. E1 under applied stress of 320 MPa with the stress ratio of 0.1 while the fatigue cycles reach 1500 and 3500. The red region is the position of maximum strain for the FSW joints. The location of maximum strain is at WNZ and the strain value at point P is 0.0079. The strain concentration remained in the WNZ until the specimen broke there.

The strain maps of specimen No. E2 under applied stress of 193.8 MPa with the stress ratio of −0.3 are shown in Figure 11. Figure 11a is the strain profile of the joint while the fatigue cycles are 120,000 and the cycle ratio is 0.55. The large strains appeared at multiple regions and were mainly distributed in the TMAZ and HAZ on both sides. Figure 11b is the strain distribution diagram of the joint when the fatigue cycles are 218,000 and the cycle ratio is 0.99. The maximum strain appeared in the BM of RS, which was consistent with the fracture location. The strain value of point Q is 0.00112. The failure location corresponds to the strain concentration area in the final fatigue stage.

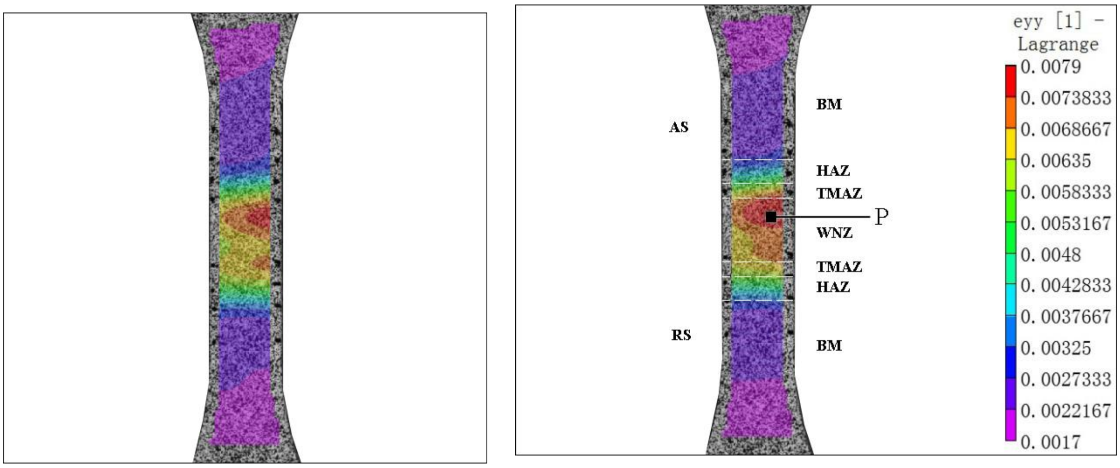

(**a**) (**b**)

Figure 10. Strain distributions of specimen under a stress ratio of 0.1 at (**a**) 1500 cycles, 42% of total life and (**b**) 3500 cycles, 98% of total life.

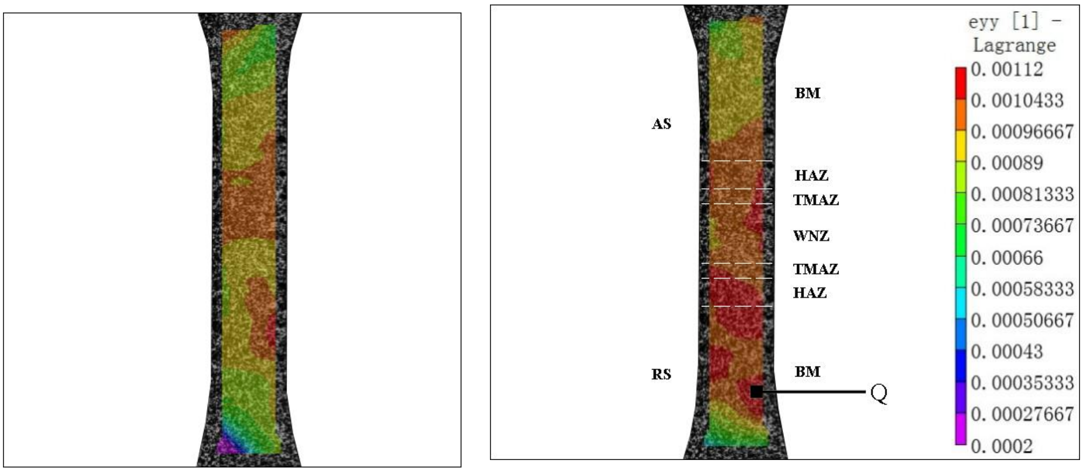

(**a**) (**b**)

Figure 11. Strain distributions of specimen under stress ratio of −0.3 at (**a**) 120,000 cycles, 55% of total life and (**b**) 218,000 cycles, 99% of total life.

The strain variation of specimen No. E1 under the maximum stress of 320 MPa with the stress ratio of 0.1 in fatigue process was analyzed. The strain data of point P in strain concentration were extracted and plotted a strain–cycle ratio curve. The strain–cycle ratio curve is shown in Figure 12. In the process of fatigue damage, the strain value has an original increase in the initial stage. It can be interpreted that it is the initial cyclic softening behavior of material. Then, before about 60% of total life, the strain increases slowly as the fatigue cycle increases. The phenomenon corresponds to the stable cyclic stage of the fatigue process and is related to the crack initiation and small crack growth in the early stage. When the fatigue cycle number reaches about 60–80% of total life, the strain of FSW joint has a little fast rise. Then, the rate of strain growth grows faster in the final stage. The phenomenon is basically consistent with the trend of fatigue crack growth rate for the FSW specimens.

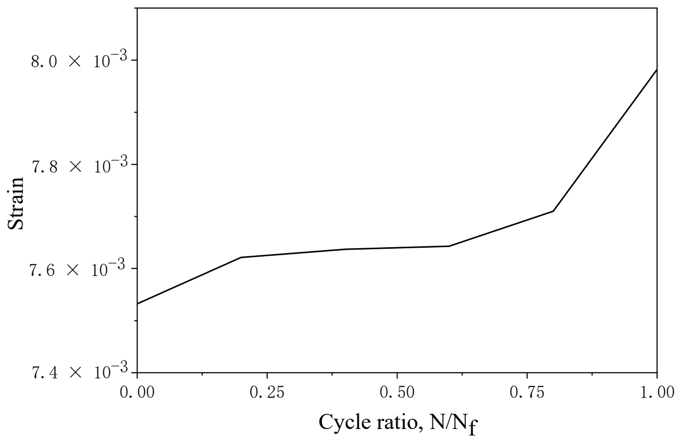

Figure 12. Strain variation of specimen in fatigue test that fractured in WNZ.

4.3. Crack Initiation and Propagation

4.3.1. Interrupted Fatigue Tests

In order to obtain the rule of small crack growth, the interrupted fatigue tests under stress control with the stress ratios of 0.1 and −0.3 and test frequency of 10 Hz were carried out with MTS-858 electro-hydraulic servo system. The experiment was interrupted by every certain cycle number and a static tensile load of 80% of the maximum stress applied to the specimen to ensure the fatigue crack being in a fully open state. Cellulose acetate film was utilized to duplicate the morphologies of cracks. About 20–30 membranes were obtained for one interrupted fatigue test. The morphologies of the cracks were also observed with a metallographic microscope. The fatigue loading conditions and results of these specimens that marked * are shown in Table 4.

For trying to obtain the rule of fatigue crack propagation in HAZ and TMAZ, other plate specimens with the finest parts in HAZ and TMAZ were designed and manufactured for interrupted fatigue tests. The diameter of the finest part of the specimens is 8 mm. The fatigue loading conditions and results of these specimens that marked ** are listed in Table 4. Among them, the finest parts of specimens D1** and D2** are HAZ and that of D3** is TMAZ. However, they all fractured at TMAZ.

4.3.2. Statics of Crack Initiation

The fatigue crack initiation and propagation characteristics in WNZ and BM were analyzed, respectively. Some hardening particles and pits in WNZ and BM became the sources of crack initiation. Most of the fatigue cracks that fractured in WNZ initiated at the hardening particle clusters, as shown in Figure 13a. Most of the fatigue cracks that fractured in BM initiated at the pits, as shown in Figures 13b and 14a. The diameter and depth of a pit in Figure 14a are about 100 and 15 μm, which is measured by laser scanning confocal microscope. The dimension of the pit is shown in Figure 14b. The cracks usually initiate at these stress or strain concentration locations and propagate perpendicular to the loading direction to both sides of the specimen [35]. From the experimental results analysis, the hardening particle cluster in WNZ has a great influence on the initiation of small cracks when the stress ratio is 0.1 and the pits in BM play an important role in the crack initiation when the stress ratio is −0.3.

4.3.3. Main Crack Growth Morphology

The main crack growth morphology in the WNZ region is shown in Figure 15a. The main crack is formed by the combination of two cracks. Two cracks initiated at point A and B, respectively. The enlarged views of crack initiation sources A and B are shown in Figure 15b,c. The initiation source of crack A is a metal streamline caused by stir welding and that of crack B is a cluster of hardening particles. Then, they propagated approximately along the direction perpendicular to the load and finally converged at point C. When a crack is hindered by the hardening particles or some defects, the path of crack propagation with least resistance will be searched, which will result in a direction transfer for the crack propagation. As shown in Figure 15, the crack propagation was hindered when the crack A encountered the hardening particle 1. A small angle deviation appeared along the crack propagation path. After that, the crack continued to propagate along the boundary of hardening particle 1. The crack morphology around hardening particle 1 is shown in Figure 15d when the fatigue cycle number is 48,000 cycles. The hardening particle 1 has dropped off and a pit is left when the fatigue cycle number reaches 54,000 cycles.

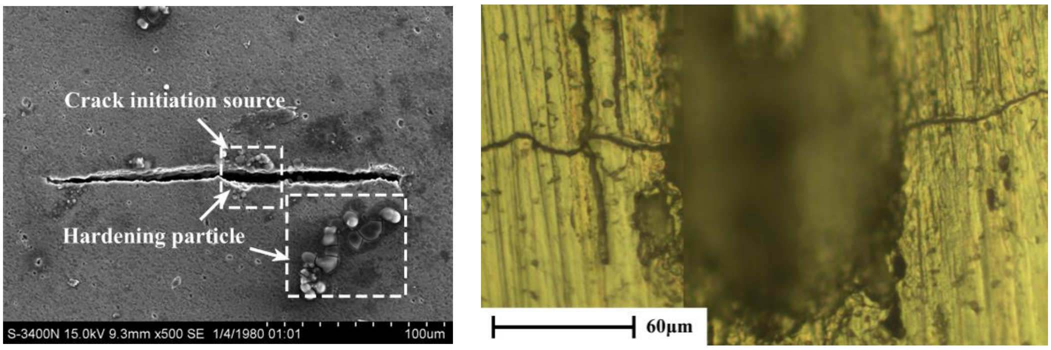

(**a**) (**b**)

Figure 13. Fatigue crack initiations at (**a**) hardening particles and (**b**) a pit.

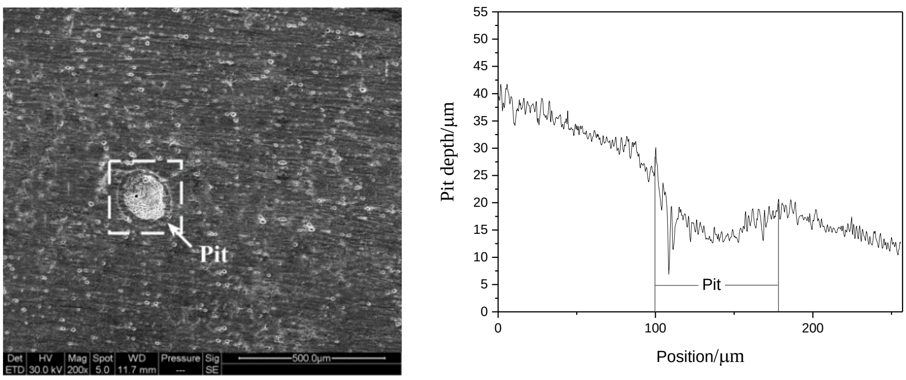

(**a**) (**b**)

Figure 14. Morphology and dimension of a pit: (**a**) morphology and (**b**) dimension measurement.

Based on the morphology of the crack growth in WNZ, the reason for the fluctuation of the crack growth rate was analyzed. The curve of crack growth rate vs. stress intensity range is shown in Figure 16. The calculation of stress intensity factor range is based on the formula proposed by Newman and Raju [36], as listed in Equation (1).

$$\Delta\mathrm{K} = \Delta\mathrm{S}\sqrt{\pi\frac{a}{Q}}F\left(\frac{a}{t},\frac{a}{c},\frac{a}{b},\varnothing\right) \tag{1}$$

where ΔS is the applied stress range, Q is a shape factor, F is a boundary-correction factor, a is the crack depth, c is the half-length of the crack, b is the half-width of the plate and t is the plate thickness, and $\varnothing$ is an parametric angle of the ellipse. The calculation of Q and F for the specimens follows the work of [36].

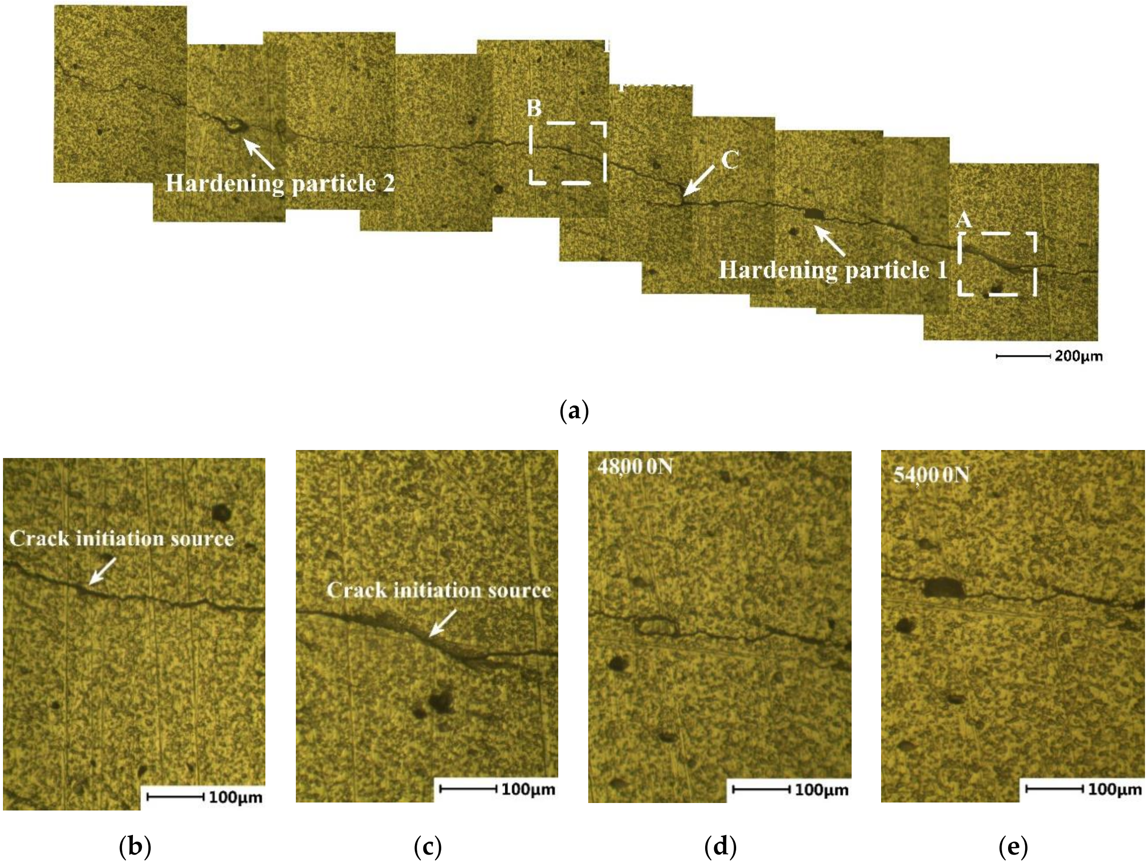

Figure 15. Crack morphology in WNZ: (**a**) main crack propagation morphology, enlarged views of (**b**) crack initiation sources B, (**c**) crack initiation sources A, (**d**) hardening particle 1 at 48,000 cycles, and (**e**) hardening particle 1 at 54,000 cycles.

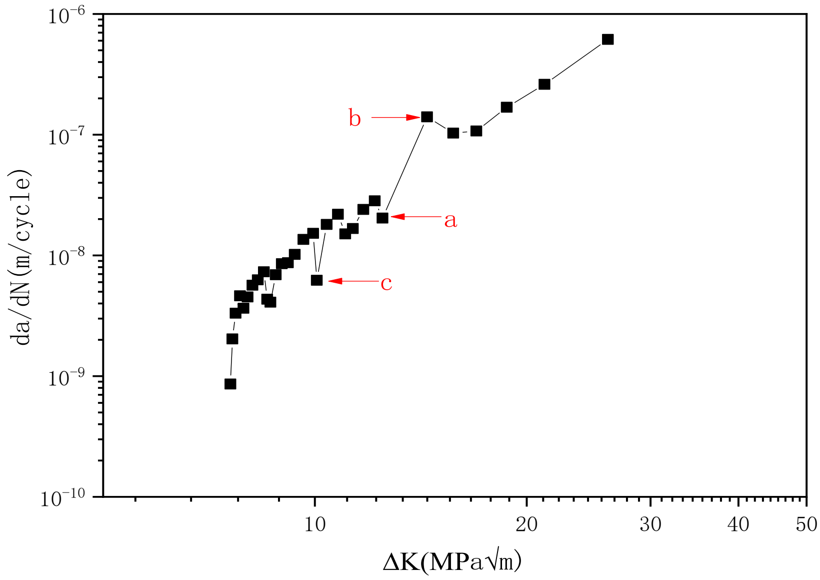

Figure 16. Crack growth rate of specimens.

The cracks A and B propagated along their respective directions when the fatigue cycle number was 43,500. The two cracks merged into the crack C when the fatigue cycle number reached 48,000. The growth rate of the crack had a significant increase from point b to a due to the combination of cracks, which is shown in Figure 16. Point c in Figure 16 showed a retardation of crack growth when crack encountered hardened particle 1. The crack growth rate increased after the crack propagated through hardening particle 1.

The metallographic morphology of the main crack growth in the BM region is shown in Figure 17. It can be seen that the crack propagation mode of BM is transgranular and the hardening particles in BM are larger than that in WNZ. Cracks initiated in a small pit on the left side of frame and extended to the right almost perpendicular to the direction of the load. Other four small cracks also initiated in the small pit apart from the main crack, as shown in Figure 17b. Five cracks propagated along their own paths in the initial stage. The four small cracks stopped in the process of propagation. Only the main crack continued to extend and ultimately caused the fracture. The direction of crack propagation had a turn when the crack encountered hardening particles 1 and 2, as shown in Figure 17c. The branching phenomenon occurred when the crack extended to the area of frame B in Figure 17a. Figure 17d is the enlarged view of the frame B. The grain boundary hindered the growth of one of the cracks.

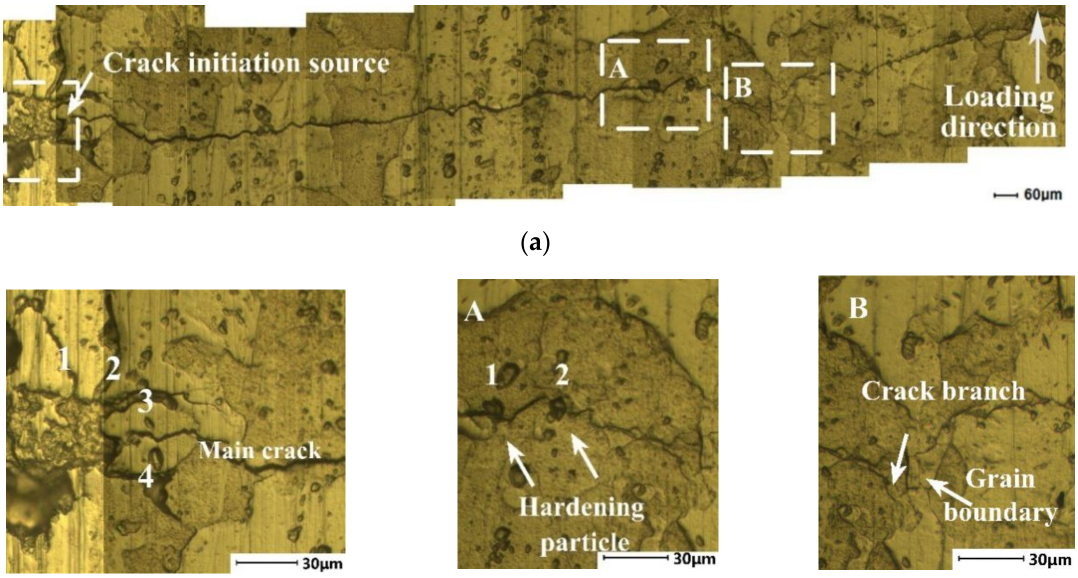

(**a**) (**b**) (**c**) (**d**)

Figure 17. Crack morphology in BM: (**a**) main crack growth morphology and enlarged views of (**b**) crack initiation source, (**c**) frame A, and (**d**) frame B.

4.3.4. Crack Growth Rate of Different Regions

The crack growth rate in different regions of FSW joints under loading stress ratio of 0.1 is shown in Figure 18. The rate of crack propagation is relatively dispersed in the early stage. Higher stress obtains higher rate of fatigue crack growth. The crack growth rate in the late stage tended to close the same under different stress levels. The crack growth rate of WNZ is significantly higher than that of TMAZ under the same stress level. It is considered that it is related to the different grain size and crack propagation mode. The cracks in WNZ propagate in an intergranular pattern and the cracks in TMAZ extend in a transgranular mode. Moreover, the Gauss texture of TMAZ is higher than that of WNZ, which also hinders the crack propagation.

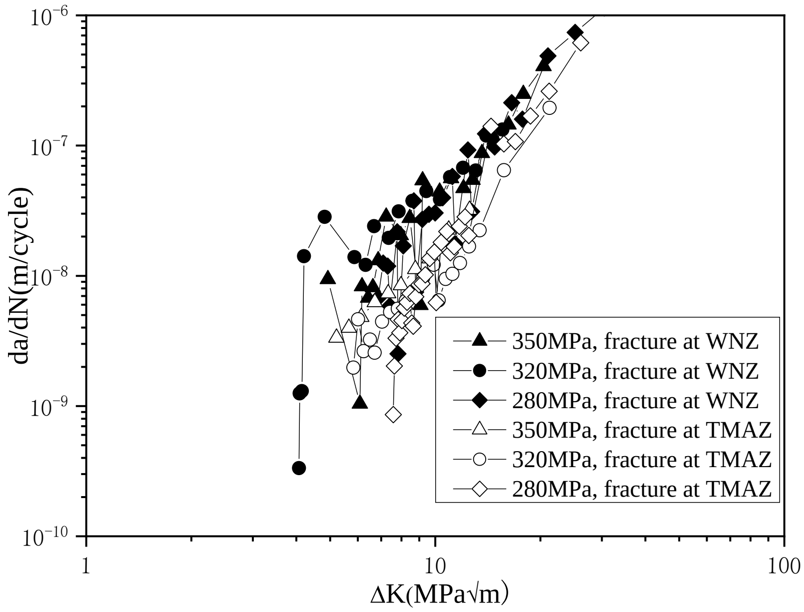

Figure 18. Crack propagation rates in different regions of the FSW joint.

5. Conclusions

The main conclusions are as follows:

1. In the tensile tests, the FSW joints broke at TMAZ, where the hardness was the lowest and deformation was large. The high contents of small angle grain boundary and shear texture in TMAZ reduces the strength of material.
2. It is found that in continuous fatigue tests, most of the FSW joints did not fracture at TMAZ, which is the weak area for tensile tests. The fatigue failure mainly occurred at WNZ when the loading stress ratio was 0.1. Most specimens broke at BM when the stress ratio was −0.3. The weak area of FSW joint will change under different loading stress conditions. The fracture occurs at a concentration of strain.
3. Most fatigue cracks in WNZ initiated at the cluster of hardening particles. However, the cracks in BM mostly initiated at the pits. The influence of hardening particle cluster and pits on the fatigue crack initiation is different in different regions.
4. The crack growth rate of WNZ is faster than that of TMAZ. It should be related to the different propagation modes of WNZ and TMAZ.

Author Contributions: X.W. and G.S. analyzed the experimental data and phenomenon; D.S., S.C., L.L. and X.H. gave some advices for the research; G.S. and X.W. wrote the paper. All authors have read and agreed to the published version of the manuscript.

Funding: This work was financially supported by National Natural Science Foundation of China (Grant No. 11672010, 51535001, U1937207).

Conflicts of Interest: The authors declare no conflict of interest.

Nomenclature

FSW	Friction stir welding
DIC	Digital image correlation
WNZ	Weld nugget zone
TMAZ	Thermo-mechanically affected zone
HAZ	Heat affected zone
HHAZ	High hardness heat affected zone

AS	Advancing side
RS	Retreating side
EBSD	Electron backscatter diffraction

References

1. Singh, V.P.; Patel, S.K.; Ranjan, A.; Kuriachen, B. Recent research progress in solid state friction-stir welding of aluminium–magnesium alloys: A critical review. *J. Mater. Res. Technol.* **2020**, *9*, 6217–6256. [CrossRef]
2. Beaudet, J.; Rückert, G.; Cortial, F. Fatigue behavior of FSW high-yield strength steel welds for shipbuilding application. *Weld. World* **2019**, *63*, 1369–1378. [CrossRef]
3. Gangwar, K.; Ramulu, M. Friction stir welding of titanium alloys: A review. *Mater. Des.* **2018**, *141*, 230–255. [CrossRef]
4. Fei, X.; Wu, Z. Research of temperature and microstructure in friction stir welding of Q235 steel with laser-assisted heating. *Results Phys.* **2018**, *11*, 1048–1051. [CrossRef]
5. Chen, Y.; Zhang, R.; He, C.; Liu, F.; Yang, K.; Wang, C.; Wang, Q.; Liu, Y. Effect of texture and banded structure on the crack initiation mechanism of a friction stir welded magnesium alloy joint in very high cycle fatigue regime. *Int. J. Fatigue* **2020**, *136*, 105617. [CrossRef]
6. Cho, J.-H.; Kim, W.J.; Gil Lee, C. Texture and microstructure evolution and mechanical properties during friction stir welding of extruded aluminum billets. *Mater. Sci. Eng. A* **2014**, *597*, 314–323. [CrossRef]
7. Bjurenstedt, A.; Ghassemali, E.; Seifeddine, S.; Dahle, A.K. The effect of Fe-rich intermetallics on crack initiation in cast aluminium: An in-situ tensile study. *Mater. Sci. Eng. A* **2019**, *756*, 502–507. [CrossRef]
8. McCullough, R.; Jordon, J.; Allison, P.; Rushing, T.; Garcia, L. Fatigue crack nucleation and small crack growth in an extruded 6061 aluminum alloy. *Int. J. Fatigue* **2019**, *119*, 52–61. [CrossRef]
9. Yan, L.; Fan, J. In-Situ SEM study of fatigue crack initiation and propagation behavior in 2524 aluminum alloy. *Mater. Des.* **2016**, *110*, 592–601. [CrossRef]
10. Wu, Z.H.; Kou, H.C.; Chen, N.N.; Hua, K.; Zhang, M.Q.; Fan, J.K.; Tang, B.; Li, J.S. The effects of grain morphology and crystallographic orientation on fatigue crack initiation in a metastable beta titanium alloy Ti-7333. *Mater. Sci. Eng. A* **2020**, *798*, 140222. [CrossRef]
11. DeBartolo, E.; Hillberry, B. Effects of constituent particle clusters on fatigue behavior of 2024-T3 aluminum alloy. *Int. J. Fatigue* **1998**, *20*, 727–735. [CrossRef]
12. Merati, A. A study of nucleation and fatigue behavior of an aerospace aluminum alloy 2024-T3. *Int. J. Fatigue* **2005**, *27*, 33–44. [CrossRef]
13. Liao, M. Probabilistic modeling of fatigue related microstructural parameters in aluminum alloys. *Eng. Fract. Mech.* **2009**, *76*, 668–680. [CrossRef]
14. Sun, G.-Q.; Wang, C.; Wei, X.; Shang, D.; Chen, S. Study on small fatigue crack initiation and growth for friction stir welded joints. *Mater. Sci. Eng. A* **2019**, *739*, 71–85. [CrossRef]
15. Shou, W.; Yi, D.; Liu, H.; Tang, C.; Shen, F.; Wang, B. Effect of grain size on the fatigue crack growth behavior of 2524-T3 aluminum alloy. *Arch. Civ. Mech. Eng.* **2016**, *16*, 304–312. [CrossRef]
16. Zheng, Z.; Cai, B.; Zhai, T.; Li, S. The behavior of fatigue crack initiation and propagation in AA2524-T34 alloy. *Mater. Sci. Eng. A* **2011**, *528*, 2017–2022. [CrossRef]
17. Sivaraj, P.; Kanagarajan, D.; Balasubramanian, V. Fatigue crack growth behaviour of friction stir welded AA7075-T651 aluminium alloy joints. *Trans. Nonferrous Met. Soc. China* **2014**, *24*, 2459–2467. [CrossRef]
18. Rajakumar, S.; Balasubramanian, V. Correlation between weld nugget grain size, weld nugget hardness and tensile strength of friction stir welded commercial grade aluminium alloy joints. *Mater. Des.* **2012**, *34*, 242–251. [CrossRef]
19. Tan, Y.; Wang, X.; Ma, M.; Zhang, J.; Liu, W.; Fu, R.; Xiang, S. A study on microstructure and mechanical properties of AA 3003 aluminum alloy joints by underwater friction stir welding. *Mater. Charact.* **2017**, *127*, 41–52. [CrossRef]
20. Deng, C.; Gao, R.; Gong, B.; Yin, T.; Liu, Y. Correlation between micro-mechanical property and very high cycle fatigue (VHCF) crack initiation in friction stir welds of 7050 aluminum alloy. *Int. J. Fatigue* **2017**, *104*, 283–292. [CrossRef]

21. Besel, Y.; Besel, M.; Mercado, U.A.; Kakiuchi, T.; Hirata, T.; Uematsu, Y. Influence of local fatigue damage evolution on crack initiation behavior in a friction stir welded Al-Mg-Sc alloy. *Int. J. Fatigue* **2017**, *99*, 151–162. [CrossRef]
22. Deng, C.; Wang, H.; Gong, B.; Li, X.; Lei, Z. Effects of microstructural heterogeneity on very high cycle fatigue properties of 7050-T7451 aluminum alloy friction stir butt welds. *Int. J. Fatigue* **2016**, *83*, 100–108. [CrossRef]
23. Besel, Y.; Besel, M.; Dietrich, E.; Wischek, J.; Mercado, U.A.; Kakiuchi, T.; Uematsu, Y. Heterogeneous local straining behavior under monotonic and cyclic loadings in a friction stir welded aluminum alloy. *Int. J. Fatigue* **2019**, *125*, 138–148. [CrossRef]
24. Li, Y.-J.; Li, Q.; Wu, A.-P.; Ma, N.-X.; Wang, G.-Q.; Murakawa, H.; Yan, D.-Y.; Wu, H.-Q. Determination of local constitutive behavior and simulation on tensile test of 2219-T87 aluminum alloy GTAW joints. *Trans. Nonferrous Met. Soc. China* **2015**, *25*, 3072–3079. [CrossRef]
25. Hatamleh, O. Effects of peening on mechanical properties in friction stir welded 2195 aluminum alloy joints. *Mater. Sci. Eng. A* **2008**, *492*, 168–176. [CrossRef]
26. Genevois, C.; Deschamps, A.; Vacher, P. Comparative study on local and global mechanical properties of 2024 T351, 2024 T6 and 5251 O friction stir welds. *Mater. Sci. Eng. A* **2006**, *415*, 162–170. [CrossRef]
27. Texier, D.; Atmani, F.; Bocher, P.; Nadeau, F.; Chen, J.; Zedan, Y.; Vanderesse, N.; Demers, V. Fatigue performances of FSW and GMAW aluminum alloys welded joints: Competition between microstructural and structural-contact-fretting crack initiation. *Int. J. Fatigue* **2018**, *116*, 220–233. [CrossRef]
28. Peng, Y.; Wu, C.; Gan, J.; Dong, J. Determination of the local constitutive properties of the welded steel joints using digital image correlation method. *Constr. Build. Mater.* **2018**, *171*, 485–492. [CrossRef]
29. Corigliano, P.; Epasto, G.; Guglielmino, E.; Risitano, G. Fatigue analysis of marine welded joints by means of DIC and IR images during static and fatigue tests. *Eng. Fract. Mech.* **2017**, *183*, 26–38. [CrossRef]
30. Malitckii, E.; Remes, H.; Lehto, P.; Bossuyt, S. Full-field Strain Measurements for Microstructurally Small Fatigue Crack Propagation Using Digital Image Correlation Method. *J. Vis. Exp.* **2019**, e59134. [CrossRef]
31. Guo, J.; Amira, S.; Gougeon, P.; Chen, X.-G. Effect of the surface preparation techniques on the EBSD analysis of a friction stir welded AA1100-B4C metal matrix composite. *Mater. Charact.* **2011**, *62*, 865–877. [CrossRef]
32. Park, S.H.C. Effect of micro-texture on fracture location in friction stir weld of Mg alloy AZ61 during tensile test. *Scr. Mater.* **2003**, *49*, 161–166. [CrossRef]
33. Jiang, X.; Chen, S.; Gong, J. Effect of non-axisymmetric arc on microstructure, texture and properties of variable polarity plasma arc welded 5A06 Al alloy. *Mater. Charact.* **2018**, *139*, 70–80. [CrossRef]
34. Gemme, F.; Verreman, Y.; Dubourg, L.; Wanjara, P. Effect of welding parameters on microstructure and mechanical properties of AA7075-T6 friction stir welded joints. *Fatigue Fract. Eng. Mater. Struct.* **2011**, *34*, 877–886. [CrossRef]
35. Fang, X.; Yan, W.; Gao, H.; Yue, Z.; Liu, J.; Wang, F. Finite element simulation of surface deformation of polycrystal with a rough surface under repeated load. *Finite Elements Anal. Des.* **2012**, *60*, 64–71. [CrossRef]
36. Newman, J.; Raju, I. An empirical stress-intensity factor equation for the surface crack. *Eng. Fract. Mech.* **1981**, *15*, 185–192. [CrossRef]